International Journal of Electrical and Computer Engineering (IJECE)
Vol. 16, No. 3, June 2026, pp. 1588~1607
ISSN: 2088-8708, DOI: 10.11591/ijece.v16i3.pp1588-1607

Hybrid deep learning (ILeS-Net) for lung cancer classification in cloud-IoT healthcare systems

Affrose[1], Cheruku Sandesh Kumar[1], Archek Praveen Kumar[2]
[1]Department of Electronics and Communication Engineering, Amity University Rajasthan, Jaipur, India
[2]Department of Electronics and Communication Engineering, Gates Institute of Technology, Anantapuramu, India

Article Info

Article history:

Received Dec 8, 2025
Revised Apr 2, 2026
Accepted Apr 26, 2026

Keywords:

Lung cancer classification
I-BIRCH
I-LGXP
Improved ILeNet-5 (ILeNet-5)
Cloud-IoT

ABSTRACT

This study presents a cloud–Internet of Things (cloud-IoT) based intelligent decision support framework for lung cancer classification and treatment recommendation, centered on a hybrid deep learning model termed ILeS-Net. Computed tomography (CT) images from a benchmark dataset are first preprocessed using Gaussian filtering to enhance image quality. Cancerous regions are identified using an Improved BIRCH (I-BIRCH) segmentation approach, followed by feature extraction using shape descriptors, color features, and Improved local Gabor XOR pattern (I-LGXP) textures. The extracted features are classified using ILeS-Net, which integrates Improved LeNet-5 and SqueezeNet architectures to achieve improved classification performance with reduced overfitting. Based on the classification results, the framework provides supportive recommendations to assist clinical decision-making. Experimental results demonstrate that the proposed ILeS-Net model achieves a maximum accuracy of 0.951, outperforming several conventional and state-of-the-art methods. The cloud–IoT integration further enables scalable, real-time, and secure data processing, highlighting the framework's potential for practical computer-aided lung cancer diagnosis.

Corresponding Author:

Affrose
Department of Electronics and Communication Engineering, Amity University Rajasthan
Jaipur, Rajasthan 303002, India
Email: roseaffrose557@gmail.com

1. INTRODUCTION

Recent technological advancements have brought about important changes across numerous industries, including healthcare [1]. Particularly important is the incorporation of cloud computing [2] and the Internet of Things (IoT) into healthcare systems [3]–[5], which has led to the development of advanced decision support systems. This merging of technologies shows great potential in transforming patient care, improving diagnostic precision, and streamlining healthcare operations. At the same time, internet of things (IoT) devices such as wearable fitness trackers, medical sensors, and intelligent monitoring devices enable remote patient monitoring, real-time data gathering, and prompt interventions, thereby promoting a patient-centered approach to healthcare delivery [6]–[8].

Despite the progress in healthcare technology, lung cancer remains a significant global health concern, with alarming rates of incidence and mortality. Annually, more than 1.8 million new cases of lung cancer are identified worldwide, leading to 1.4 million deaths [9], [10]. Lung cancer holds the highest mortality rate among various types of cancer, highlighting the critical necessity for efficient detection and treatment approaches [11], [12].

Acknowledging the difficulties linked to diagnosing lung cancer, especially the lack of symptoms in its early phases, alongside factors like respiratory problems and smoking history, highlights the crucial

significance of early detection. Conventional diagnostic imaging methods such as computed tomography (CT), positron emission tomography (PET), and magnetic resonance imaging (MRI) face constraints in identifying lung masses, prompting the exploration of innovative technologies to fill these gaps [13], [14].

To tackle these challenges, scientists have progressively embraced artificial intelligence (AI) and machine learning (ML) methodologies to create inventive solutions for detecting lung cancer. AI's expertise in computer vision, big data analysis, and healthcare utilization positions it favorably for tackling classification issues in medical imaging [15]. Within this framework, a cloud-IoT decision support system based on DL [16], [17] emerges as a compelling strategy to enhance lung cancer detection and advance patient outcomes.

Utilizing AI, cloud computing, and IoT technologies, this system aims to exceed the constraints of conventional diagnostic techniques, equipping healthcare providers with instant insights and practical recommendations for early detection and intervention. This research outlines the structure of a deep learning-based cloud-IoT decision support system designed for lung cancer classification. As a result, the proposed model presents four unique contributions, each methodically explained as follows.

- Proposing I-BIRCH to provide an effective segmentation via incorporating automated threshold initialization and improved distance matrices for enhancing the clustering accuracy, memory utilization, and time complexity by effectively adapting to extensive datasets.
- Extracting I-LGXP-based features in addition to conventional shape and color features from the segmented image to provide an accurate lung cancer classification. This I-LGXP is an enhanced feature, where, the parameters are adjusted which enhances the filter's ability to distinguish between various texture patterns in images, improving overall image quality and analysis accuracy.
- Proposing ILeS-Net model, which is the hybridization of ILeNet-5 and SqueezeNet models to provide better lung cancer classification. Here, ILeNet-5 model is the conventional LeNet-5 model's improved version, where the model's stability and efficiency are enhanced during training via incorporating Improved BN layer and Hard Elish Swish maxout activation function.

The rest of this study is constructed as follows: Section 2 reviews on previous study within the domain of lung cancer. Following that, section 3 explores the process of the proposed ILeS-Net framework. Section 4 presents the evaluation findings and presents a comprehensive discussion. Finally, section 5 encapsulates the study's findings and conclusions.

2. LITERATURE REVIEW

This section provides a concise overview of lung cancer classification by synthesizing insights from ten relevant research papers. In 2023, Faruqui *et al.* [18] has introduced healthcare-as-a-service (HAAS) model inspired by software-as-a-service (SAAS) within the cloud computing paradigm. In 2023, Tomassini *et al.* [19] have developed a LUCY advanced on-cloud decision support system from thorax CT scans. In 2020, Hwang *et al.* [20] has compared the CT interpretation before and after implementation of a computerized system for lung nodule detection. In 2019, Masood *et al.* [21] have developed a 3DDCNN for lung nodule detection based on assisting the radiologists. In 2022, Kasinathan and Jayakumar [22] has presented a Cloud-LTDSC a hybrid technique for PET/CT images classifying and validating different stages of lung tumor progression. A novel SCMO-MLL2C method was introduced by Valluru and Jeya [23] in 2020 for use with CT scans. In 2020, Masood *et al.* [24] has suggested an enhanced mRFCN based automated decision support system for lung nodule detection and classification. Utilizing mRFCN as the image classifier backbone for feature extraction and mLRPN with PSSM was integral. Additionally, a deconvolutional layer was introduced to incorporate the suggested mLRPN into this framework, facilitating the automatic selection of potential ROI. In 2021, Mishra *et al.* [25] have developed a sustainable lung cancer detection model to integrate the IoHT and computational intelligence, causing the least harm to the environment. In 2023, Raza *et al.* [26] has presented a transfer learning (TL) based predictor called Lung-EffNet for lung cancer classification. Constructed based on the EfficientNet architecture, it was further enhanced by incorporating additional top layers in the classification head of the model. In 2024, Gomiasti *et al.* [27] have enhanced the efficiency of lung cancer classification performance via support vector machine (SVM) with hyperparameter tuning. In 2024, Amin *et al.* [28] has proposed multimodal non-small cell lung cancer (NSCLC) classification using CNN model. From the genomic data commons (GDC) portal data was gathered and then diverse pre-processing techniques were utilized for preparing the genomic as well as slide images. In 2024, Noman *et al.* [29] has proposed LungCT-NET, which was a TL-based architecture coupled with EL for the lung nodule categorization. In 2025, Zhao *et al.* [30] has proposed PortNet, which was developed for reducing the model's parameter size along with attaining the lightweight characteristics without compromising the categorization accuracy. In 2023, Sun *et al.* [31] proposed Swin Transformer for classification as well as segmentation of lung cancer. In 2024, Imran *et al.* [32] proposed CNN-ViT for NSCLC detection and classification. The NSCLC was categorized into normal, squamous cell carcinoma and adenocarcinoma by this model.

3. PROPOSED ILES-NET POWERED CLOUD-IOT FRAMEWORK FOR INTELLIGENT LUNG CANCER DETECTION AND RECOMMENDATIONS

Arising from the uncontrolled growth of abnormal cells in lung tissues, lung cancer stands as one of the most prevalent and deadly types of cancer worldwide. Lung cancer classification aims to differentiate these subtypes and identify specific characteristics of the tumor, such as size, location, and histological features, which can inform treatment decisions and prognosis. Conventional methods for lung cancer classification typically rely on histopathological examination of tissue samples obtained through invasive procedures like biopsies or surgical resection. But these methods may not fully capture the molecular and genetic complexities of lung cancer, which are increasingly recognized as important factors in cancer behavior and treatment response. Additionally, medical imaging techniques such as CT, X-rays, and MRI are used to visualize the lung and detect abnormalities. Radiologists interpret these images to identify suspicious lesions, assess tumor size and location, and guide treatment planning. Accordingly, ILeS-Net powered cloud-IoT framework for intelligent lung cancer detection and recommendations is proposed in this work. Initially, the acquired CT images are processed by Gaussian filtering in the pre-processing stage. Following this, segmentation using I-BIRCH is employed to segment the cancerous portion from the pre-processed CT images. Then, the segmented images are subjected to feature extraction stage to acquire the pertinent features. This procedure includes retrieving shape features, I-LGXP, and color features from the segmented image. Next, the retrieved features are fed as input to the hybrid model, comprisingILeNet-5 and SqueezeNetis presented for lung cancer classification. Based on the classification outcome, recommendation on patient treatments is suggested. Figure 1 illustrates the cloud-IoT based lung cancer classification and recommendation model.

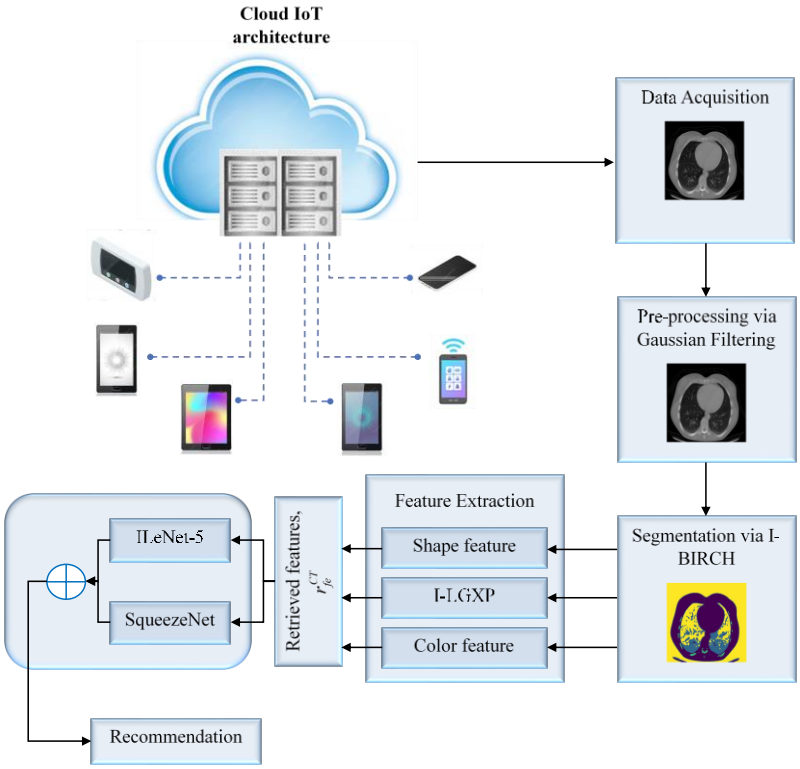

Figure 1. Overall architecture of the lung cancer classification and recommendation model

3.1. Data acquisition

In the data acquisition stage, CT images are captured using IoT devices and stored in cloud. These IoT devices are equipped with sensors capable of capturing detailed images of the lungs, providing valuable data for analysis. The captured CT images i^{CT} serve as input for a DL-based cloud-IoT decision support system specifically designed for lung cancer classification. The process includes preprocessing the CT images to enhance their quality and remove noise, ensuring accurate classification results. Each captured

image is represented as part of the input CT images denoted as $i^{CT} = (i_1^{CT}, i_2^{CT}, \ldots, i_n^{CT})$, where $n$represents the total number of captured images. Through this comprehensive data acquisition process, the system aims to utilize the wealth of information gathered from IoT devices to improve early detection and classification of lung cancer, eventually contributing to more efficient patient care and treatment outcomes. According to this work, we are considering benchmark dataset to get the CT images.

3.2. Gaussian filtering technique-based pre-processing

In this stage following data acquisition of CT images i^{CT}, several key steps are undertaken to ensure that the raw data obtained from the imaging equipment is optimized for subsequent analysis. Initially, the acquired CT images i^{CT} may suffer from various artifacts and noise, which can obscure important features relevant to lung cancer detection. So, pre-processing this image is essential. Therefore, we have utilized the noise reduction technique like Gaussian filtering to enhance CT image i^{CT} quality while preserving critical anatomical details.

Moreover, Gaussian filtering is widely employed in image processing to diminish noise and achieve smoothing effects. When applied to pre-processing stage, the Gaussian filtering enhances the input CT image i^{CT} quality by minimizing noise while retaining crucial features essential for accurate classification. This technique involves the convolution of the image with a Gaussian kernela bell-shaped curve reflecting the value distribution. Essentially, Gaussian filtering performs a linear filtering operation aimed at blurring or smoothing the image. By benefit of its convolution process with the Gaussian kernel, this technique effectively reduces high-frequency noise in the CT image i^{CT} while maintaining the important features, crucial for subsequent classification tasks. Equation (1) explain the gaussian kernel [33].

$$Gaussian(a,b) = \frac{1}{2\pi St^2} e^{-\frac{a^2+b^2}{2St^2}} \quad (1)$$

Equation (1), the coordinates (a,b) are relative to the center of the kernel, $Gaussian(a,b)$ denotes the gaussian function value at coordinates (a,b), St determines the width of the kernel by serving as the standard deviation of the Gaussian distribution. Hence, the output achieved from this pre-processing stage is denoted as p^{CT}.

3.3. Improved BIRCH based segmentation

After preprocessing stage, the segmentation procedure focuses on segmenting the diseased regions from lung cancer images. This algorithm offers enhanced efficiency in shape analysis by improving the distance function used for evaluating pixel distances, thereby enabling more accurate segmentation of diseased regions. Specifically, the I-BIRCH algorithm consists of four stages, with improvement made in two stages to ensure its effectiveness for the lung cancer classification. A detailed depiction of the proposed I-BIRCH algorithm's flow can be established in Figure 2, providing a concise yet comprehensive overview of its operation and significance within the segmentation procedure for lung cancer CT images.

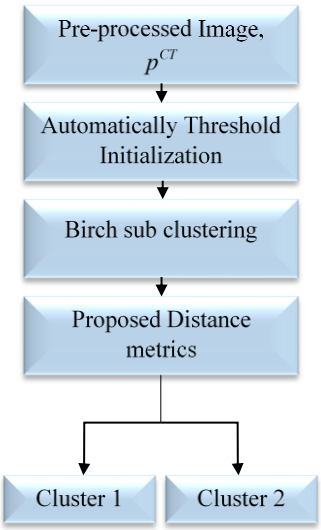

Figure 2. Flowchart of I-BIRCH based segmentation

a. Pre-processing the image: By the way, the pre-processed image p^{CT} undergoes additional pre-processing within the I-BIRCH algorithm. Key features pertinent to classification are selected, fitted into corresponding cluster labels and any identified outliers are eliminated via feature rescaling.
b. Automated initialization of threshold: In the conventional threshold initialization method, data points that exceed the threshold are adjusted to the threshold value. This adjustment is achieved by expanding the scale of the leaf radius, aiming to decrease the split parent in the proposed birch model [34]. Consequently, the automatic initialization of the threshold achieves through an enhanced threshold, which is employed to assess uncertainties, as described in (2).

$$Threshold_{Imp} = \left\{ \begin{array}{l} \left[v_1 (\upsilon_1 - \upsilon)^2 * \left(-\sum_{F \subseteq \theta} m(F) \log_2 \frac{\frac{m(F)}{2^{|A|}-1}}{.e^{\frac{|F|-1}{|C|}}} \right) \right] + v_2 (\upsilon_2 - \upsilon)^2 * / \\ \left[-\sum_{F \subseteq \theta} m(F) \log_2 \frac{\frac{m(F)}{2^{|A|}-1}}{.e^{\frac{|F|-1}{|C|}}} \right] / \left[-\sum \mathrm{P}(p^{CT}) \log_b \mathrm{P}(p^{CT}) \right] \end{array} \right\} \quad (2)$$

From (2), $v_1 = \sum_{i=0}^{k} P_i \, v_2 = \sum_{i=k+1}^{k-1} P_i$, $\upsilon_1 = \frac{1}{v_1} \sum_{i=0}^{k} iP_i$, $\upsilon_2 = \frac{1}{v_2} \sum_{i=0}^{k-1} iP_i$ and $\upsilon_1 = \sum_{j=0}^{i-1} iP_i$, υ defines the image overall gray value, υ_i explains the average value of gray level of the pixel, $b = 2$, F denotes the focal element of m, mass function is indicated by m, $|F|$ cardinality of F, and $|C|$cardinality of belief of entropy C.

c. Birch sub clustering: During the sub-clustering stage, each patient's data point, representing various features such as tumor size, location, and histopathological characteristics, is assigned to a sub-cluster based on its similarity to the centroid of that sub-cluster. This proximity is typically measured using distance metrics like Euclidean distance or cosine similarity. By iteratively assigning data points to the nearest sub-cluster centroid, the algorithm gradually refines the segmentation, effectively breaking down larger, heterogeneous clusters of lung cancer cases into smaller, more homogeneous groups.
d. Altering distance metrices in the baseline birch: Conventionally, the distance [35] is calculated as given in (3).

$$Dist = \sum_{i=1}^{n} min(|e_i - f_i|, q - |e_i - f_i|) \quad (3)$$

While effective for large datasets, this method may face challenges with computational resources and scalability when dealing with extremely large or high-dimensional data. Therefore, the distance is improved by combining the Improved Lee distance and Euclidean distance as expressed in (4).

$$Dist_{imp} = \left\{ \frac{\sum_{i=1}^{n} min(|e_i - f_i|, q - |e_i - f_i|)}{min\left(\sqrt{\sum_{i=1}^{n} (e_i)^2}, \sqrt{\sum_{i=1}^{n} (f_i)^2} \right) + q(|e_i - f_i|)} \right\} + \sqrt{\sum_{i=1}^{n} (e_i - f_i)^2} \, /2 \quad (4)$$

Equation (4), e_i, f_i represent pixels that are adjacent to one another. This improvement optimizes clustering accuracy, memory usage, and time complexity by efficiently scaling to large datasets.

The final step in I-BIRCH involves outputting the clusters, typically denoted as cluster 1, cluster 2. These clusters represent the final segmentation of the dataset based on the clustering performed by the I-BIRCH. After obtaining the clusters, the segmented image can be generated by assigning each pixel in the original image to the cluster it belongs to. Each cluster represents a distinct region or group of pixels in the image that share similar characteristics. Thus, the output achieved from this I-BIRCH based segmentation is implied as s^{CT}.

3.4. Feature extraction

After segmentation, from the segmented image s^{CT}, relevant features are extracted. This process aims to capture distinctive features of the segmented regions, which aids in distinguishing healthy and cancerous tissue. Typically, features like shape features, Improved LGXP based feature, and color features are retrieved. Each feature captures diverse information about the lung nodules. Therefore, extracting shape, I-LGXP, and color features allows the classifier to understand what pattern a nodule has and how the nodule looks and what density it has. With these details, the classification is conducted. Extracted each feature is detailed.

3.4.1. Shape features

Shape features play a vital role in characterizing the geometric properties of the segmented regions by inputting the segmented image s^{CT}. It refers to characteristics or descriptors derived from the shapes of regions within the segmented lung images. Here, certain geometric characteristics such as area, moment, perimeter, epsilon, and convexity are being retrieved as the shape feature.

- Area: It quantifies the total number of pixels within each segmented region [36] and its expression is provided in (5).

$$Area = \sum_{c=1}^{n} \sum_{d=1}^{m} s^{CT}(c,d) \quad (5)$$

  here, image size is denoted as n, m, spatial coordinates are represented as c, d.
- Moment: Moments are mathematical descriptors that capture different aspects of the shape and spatial distribution of pixels within a segmented area.
- Perimeter: The perimeter feature measures the total length of the boundary or outline of the segmented region [36] as defined by (6).

$$Perimeter = \sum_{i=1}^{n} \sqrt[2]{(c_1 - c_{i-1}) + (d_1 - d_{i-1})} \quad (6)$$

  here, the i-th pixel of the spatial coordinates is represented as c, d.
- Epsilon: Epsilon ε is a parameter used in shape analysis to define the maximum allowable distance between a contour and its approximation.
- Convexity: Convexity measures the degree to which a segmented region is convex or concave in shape.

Thus, the output attained from this shape feature is specified as $Shape_{fe}^{CT}$.

3.4.2. Improved LGXP based feature

LGXP is a feature descriptor that focuses on encoding local gradient information and incorporating XOR patterns to represent texture variations within the segmented regions. During this process, the segmented images s^{CT} are analyzed at a local level to compute gradient information, which provides insights into the intensity changes across neighboring pixels. This concept encompasses five primary stages contains image acquisition, noise suppression, improved gradient computation, LGXOR, and histogram of image [37]. Thereby, the flowchart illustrating the procedure of the ILGXP is depicted in Figure 3.

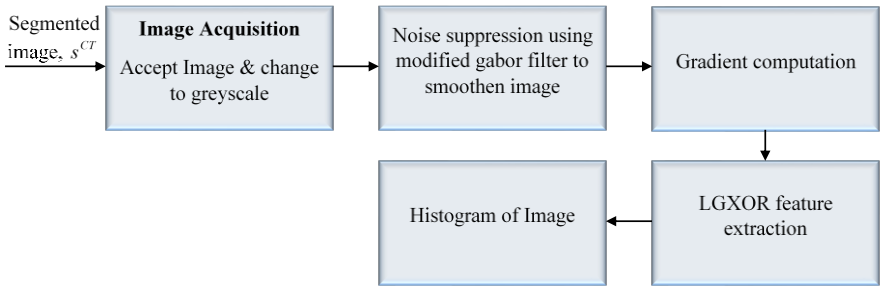

Figure 3. Flowchart of Improved LGXP

a. Image acquisition

The input segmented image s^{CT} is converted into a grayscale image (non-colored), simplifying the analysis process. The intensity of this grayscale image ranges from 0 to 255. Therefore, the expression for the grayscale image is elucidated as follows:

An image is comprised of pixels organized in rows and columns to describe its dimensions. The width and height of each column and row in an image are determined by its resolution. The image total number of pixels is meant as $np^i nq^j$ that signifies its dimensions. Pixels intensity matrix positioned at coordinates (pi, qi) within the digital image is utilized to represent it, where np indicates width and nq indicates height. Take $Int_{ij}(i = 1,2,3,..,n, j = 1,2,3,..,n)$ as grayscale, here Int_{ij} represents the digital image's intensity at the specified position... (i,j). The image may be subject to fluctuating noise $Noise_{ij}$, affecting the pixel at location (i,j). Consequently, the combined setting, as expressed in (7), is employed to define the image's gray level intensity. Thus, the grayscale image can be represented as $Gray^s(p,q)$.

$$Gray_{i,j}^{s} = Int_{i,j} + Noise_{i,j} \tag{7}$$

b. Noise suppression

Firstly, the grayscale image $Gray^{s}(p,y)$ is fed as input to the Gabor filter. This combination has established optimistic outcomes. Gabor filter characterized as bandpass filters, that selectively allow a specified range of frequencies to pass through. Mathematically, a 1D Gabor filter is represented as convolution of a function sinusoidal, as described in (8), with a Gaussian function. Here, fr and φ denote the sinusoidal wave's frequency and phase offsets, while Wl and σ_p represent the wavelength and standard deviation along the x-axis of the Gabor function.

$$Gray^{s}(p) = exp\left(-\frac{p^2}{2\sigma_p^2}\right) exp\left(i\left(\frac{2\pi p}{fr} + \varphi\right)\right)$$
$$e^{ip} = cos\, p + i\, sin\, p\,, \left(i = \sqrt{-1}\right) \tag{8}$$

Given that the image signifies a 2D function, equation (8) has been adjusted to (9), where the real and imaginary parts are denoted as $Gray^{s}(p,q) = exp\left(-\frac{p^2+S^2p^{i2}}{2\sigma^2}\right) cos\left(\frac{2\pi p^{i}}{fr} + \varphi\right)$ and $Gray^{s}(p,q) = exp\left(-\frac{p^2+S^2q^{i2}}{2\sigma^2}\right) sin\left(\frac{2\pi p^{i}}{fr} + \varphi\right)$. Here, $p^{i} = p\, cos\, \theta + q\, sin\, \theta\,;\ q^{i} = -p\, sin\, \theta + q\, cos\, \theta$. Also, the conventional real part is given in (10).

$$Gray^{s}(p,q) = exp\left(-\frac{p^2+S^2q^{i2}}{2\sigma_p^2}\right) exp\left(i\left(\frac{2\pi p^{i}}{fr} + \varphi\right)\right) \tag{9}$$

$$Gray^{s}(p,q;S,\kappa,\theta,\varphi) = exp\left(-\frac{p^2+S^2q^{i2}}{2\sigma^2}\right) cos\left(\frac{2\pi p^{i}}{\kappa} + \varphi\right) \tag{10}$$

However, excessive parameter adjustments may lead to overfitting, causing the filter to become too specialized and potentially less effective at recognizing broader patterns or variations in textures. Thus, the real part of the grayscale is enhanced in this I-LGXP [38] as provided in (11).

$$Gray^{s}(p,q;S,\kappa,\theta,\varphi) = exp\left(-\frac{p^2+S^2q^{i2}}{2\sigma^2}\right) cos\left(\frac{2\pi p^{i}}{\kappa} + \varphi\right).\left[\frac{2\pi M_{p,q} D(p,q)}{tan\left(\frac{2\pi q^{'}}{\kappa}\right)}\right] \tag{11}$$

In (11), the $M(p,q) = \frac{\sum_{i=1}^{n} 2(p^{i}-q^{i})^{2}}{\sum_{i=1}^{n}(p^{i}+q^{i})} + \frac{\sigma}{\mu} * 100$, $p^{i} = p\, tan\, \theta + q\, sin\, \theta$, $q^{i} = -p\, cos\, \theta + q\, cot\, \theta$, $D(p,q) = \left[\frac{\sum_{j=1}^{m}(p^{i}-\bar{p}^{i})(q^{i}-\bar{q}^{i})}{\sqrt{\sum_{j=1}^{m}(p^{i}-\bar{p}^{i})^{2}\sum_{j=1}^{m}(q^{i}-\bar{q}^{i})^{2}}}\right]$, $\bar{p}^{i}, \bar{q}^{i}$ denotes the average value. By adjusting the parameters enhances the filter's ability to distinguish between various texture patterns in images, improving overall image quality and analysis accuracy.

Mathematically the grayscale image is represented by combining it with the Gabor filter to filter out undesirable data. This filtering process σaims to blur the image. Considering images input and output of the filter are denoted as $Gray^{s}(p,q)$ and $Gray^{s^{'}}(p,q)$, Figure 4 illustrates a potential smoothing arrangement.

c. Gradient computation

The main process is on computing gradients and pixel points identification with the highest change in grayscale intensity, also the Sobel operator being used to compute gradients. This operator operates in 2D, specifically in the i and j directions. Equation (12) represents the matrices for the Sobel operators in these two directions are D_i and D_j.

$$D_i = \begin{bmatrix} -1 & 0 & +1 \\ -2 & 0 & +2 \\ -1 & 0 & +1 \end{bmatrix}$$
$$D_j = \begin{bmatrix} -1 & +2 & +1 \\ 0 & 0 & 0 \\ -1 & -2 & -1 \end{bmatrix} \tag{12}$$

In (12), D_i and D_j specifies the matrices which are convolved with the blurred image pixels $Bl(i,j)$ in the i and j directions, respectively. The pixel point gradient at (i,j) is given in (13) and (14).

$$Gr_i = D_i * Bl(i,j) \tag{13}$$

$$Gr_j = D_j * Bl(i,j) \tag{14}$$

Equation (15) calculates the magnitude of the edge, that is denoted as $edge$.

$$edge = \sqrt{Gr_i^2 + Gr_j^2} \tag{15}$$

The arctan of the ratio between Gr_j and Gr_i provides the computed gradient directions at the pixel point (i,j).

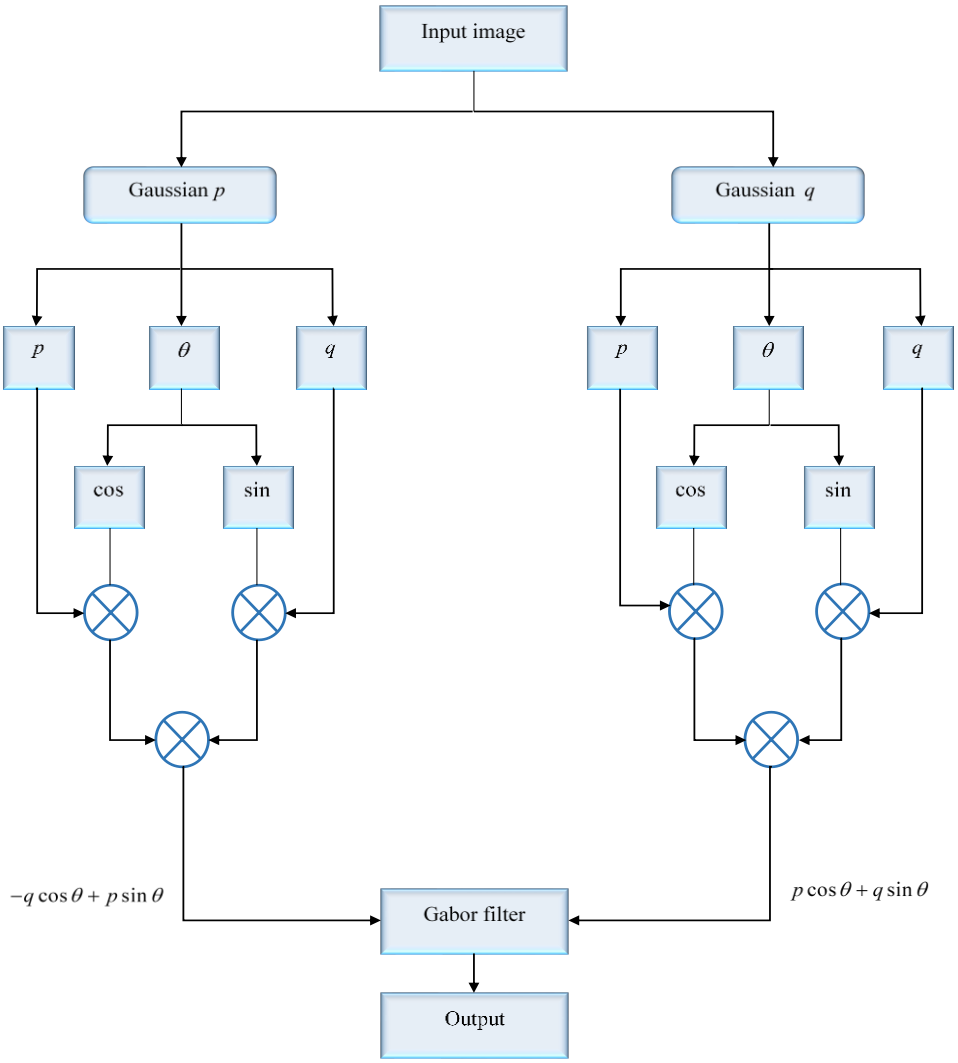

Figure 4. Image is smoothed through noise suppression using a modified Gabor filter

d. LGXOR

After computing the gradient, LGXOR features are retrieved. For lung cancer classification, Gabor filters demonstrate considerable efficiency and adequacy in capturing their individual features. Both bandpass and Gabor filters are employed to extract features. This representation involves concatenating significant binary variables derived from the primary image pixels.

e. Histogram of image

I-LGXP involves obtaining the histogram of the image in the final stage. The histogram of image is derived from LGXOR retrieved feature's output. Equation (16) represents a mathematical equation for detailing how these features are partitioned into sub-blocks. Here, $Hist_{v,\varphi,j}$ signifies the histogram of the j^{th} sub-block of the $(j = 1,2,..,l)$ LGXOR map. Two LGXOR descriptors for lung cancer, denoted as $Hist^1$ and $Hist^1$ are evaluated according to (17). Equation (18) illustrates the operation of histogram intersection; the total amount of histogram bins is indicating as h^{bins}.

$$Hist = \left[Hist_{\varphi 0,v0,1},\ldots,Hist_{\varphi 0,v0,l};Hist_{\varphi 0-1,v0-1,l},..,H_{\varphi 0-1,v0-1,l}\right] \quad (16)$$

$$S'(Hist^1,Hist^2) = \sum_{\varphi=\varphi 0}^{\varphi_{o-1}}\sum_{v=v0}^{v_{s-1}}\sum_{j=1}^{l}\cap\left(Hist_{v,\varphi,j}^1,Hist_{v,\varphi,j}^2\right) \quad (17)$$

$$\cap\left(Hist^1,Hist^2\right) = \sum_{j=1}^{h^{bins}} min\left(h_i^1,h_i^2\right) \quad (18)$$

Thus, the I-LGXP output achieved from this stage is implied as $I - LGXP_{fe}^{CT}$.

3.4.3. Color features

When analyzing segmented CT images, color features like color histogram, mean, median, and skewness provide valuable insights into the distribution and characteristics of pixel intensities within the segmented regions. Here, the segmented images^{CT} is given as an input for retrieve the Color features.

a. Color histogram: This feature represents the frequency distribution of pixel intensities within the segmented region across different color channels [39]. It shows how prevalent each intensity level is, providing an overall view of the color distribution as described by (19).

$$C^{Histogram} = \{h_i[C_1],h_i[C_{12}],\ldots\ldots,h_i[C_k] = 1{,}0 \le h_i[C_k] \le 1\} \quad (19)$$

The frequency of pixels is denoted as $h_i[C_k]$, corresponding to the k-th color present in the image is described in (20).

$$h_i[C_k] = \frac{\sum_{i=0}^{W_1-1}\sum_{j=0}^{W_2-1}\begin{cases}1\left(s^{CT}(i,j)=C_k\right)\\0(other)\end{cases}}{W_1\times W_2} \quad (20)$$

In (20), the image width is denoted by W_1 and the image height is signified by W_2.

b. Mean: It is a measure of the average brightness or color value [40] and its expression is defined in (21).

$$Mean_{color} = \frac{1}{AB}\sum_{i=1}^{A}\sum_{j=1}^{B}V_{ij}^{color} \quad (21)$$

From (21), A and B means the dimension of the image and color value is denoted by V_{ij}^{color} on column i and row j.

c. Median: It denotes the median value within the sorted list of pixel intensities within the segmented area.

d. Skewness: It evaluates the asymmetry of the pixel intensity distribution within the segmented region. Skewness can provide insights into the shape and uniformity of the color distribution [40] and its mathematical calculation is described in (22).

$$Skewness_{color} = \frac{\sum_{i=1}^{A}\sum_{j=1}^{B}\left(V_{ij}^{color}\right)^3}{ABStandarddeviation} \quad (22)$$

Thus, the output gotten from this shape feature is meant as, $Color_{fe}^{CT}$. Lastly, the relevant features like shape features $Shape_{fe}^{CT}$, I-LGXP$I - LGXP_{fe}^{CT}$, and color features $Color_{fe}^{CT}$ are retrieved. Therefore, the retrieved features are indicated as, r_{fe}^{CT}.

3.5. Lung cancer classification using ILeS-Net model

Lung cancer classification is an essential stage in this proposed ILeS-Net model. The retrieved features r_{fe}^{CT}, serves as input for classifying lung cancer. To achieve this task, a novel hybrid ILeS-Net model is introduced and utilized for classifying lung cancer. This hybrid model combines the ILeNet-5 and

SqueezeNet as shown in Figure 5 presents a comprehensive model for classifying lung cancer. Subsequent sections will provide detailed explanations of these two classifiers.

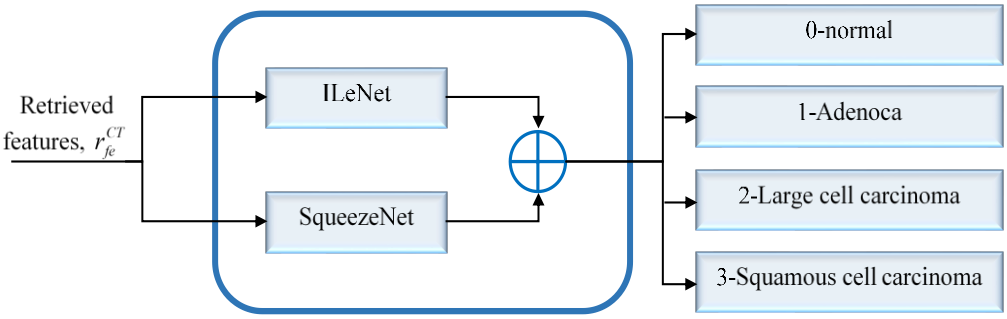

Figure 5. Proposed hybrid ILeS-Net model for lung cancer classification

3.5.1. Procedural explanation of ILeNet-5 model

Conventionally, the LeNet-5 [41] architecture is the effective process for cancer classification via CT images. This LeNet-5 model contains of two convolutional layers, two average pooling layers, and FC layer with retrieved features r_{fe}^{CT} as input as shown in Figure 6.

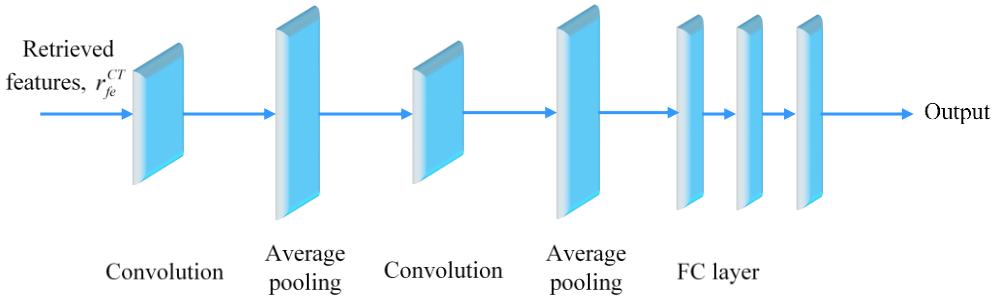

Figure 6. Conventional LeNet-5 model

The convolutional layers are responsible for detecting important patterns and features indicative of lung abnormalities, such as tumor masses or irregularities in tissue density. The output from these layers is then fed into FC layers, where the high-level features are learned and mapped to the output classes.

In this ILeS-Net model, an ILeNet-5 architecture is proposed, comprising several key components. It begins with a convolutional layer followed by improved batch normalization and stochastic pooling. Subsequently, another convolutional layer is employed, succeeded by improved batch normalization and average pooling. Following this, another convolutional layer with improved batch normalization is utilized, followed by stochastic pooling. The model further employs scale dot product operations, an FC layer and an improved activation function for enhanced performance in classification tasks. Thus, the detailed procedural explanation for each layer in the ILeNet-5 model is given below and its pictorial representation is depicted in Figure 7.

a. Convolutional layer (convolution): This layer applies convolutional filters to the input retrieved features r_{fe}^{CT}, which allows the network to learn spatial hierarchies of features. Each filter convolves across the input image, capturing different patterns.
b. Improved batch normalization: It normalizes the activations [42] of the previous layer across the mini-batch. Equation (23) explains the conventional batch normalization.

$$Output_{B,ch,y,x} \leftarrow \vartheta_{ch} \frac{Input_{B,ch,y,x} - Mean_{ch}}{\sqrt{Std_{ch}^2 + \epsilon}} + \delta_{ch} \forall B, ch, y, x \quad (23)$$

In (23), $Mean_{ch} = \frac{1}{|b|}\sum_{B,y,x} Input_{B,y,x}$ defines the mean activation, B denotes the batch, ch implies the channel, spatial dimensions are y, x, b comprises all activations in channel ch across all features B in the entire mini-batch, encompassing all spatial locations $y$and x, ϑ, δ refers the parameters, $\in$ is done for numerical stability and Std means the standard deviation. In this ILeNet-5 model, the mean activation term is improved in the batch normalization as given in (24). This enhancement involves incorporating the contra-harmonic mean and interquartile mean by dividing the minimum of the arithmetic and geometric mean into the mean activation term. Thus, the mean and variance of each feature independently across the entire batch. Which aims to improve its stability and convergence during training.

$$Mean_{ch} = \left[\frac{CM+IQ}{min(AM,GM)}\right] \tag{24}$$

From (24), $CM = \frac{h_1^2+h_2^2+\ldots+h_n^2}{h_1+h_2+\ldots+h_n}$ means the contra harmonic mean, $IQ_{Mean} = \frac{2}{n}\sum_{i=\frac{n}{4}+1}^{\frac{3n}{4}} r_{fe}^{CT}$ refers to the interquartile mean, $AM = \frac{1}{n}\left(\sum_{i=1}^{n} r_{fe}^{CT}\right)$ describes the arithmetic mean, and $GM = \sqrt[n]{h_1.h_2.\ldots.h_n}$ defines the geometric mean.

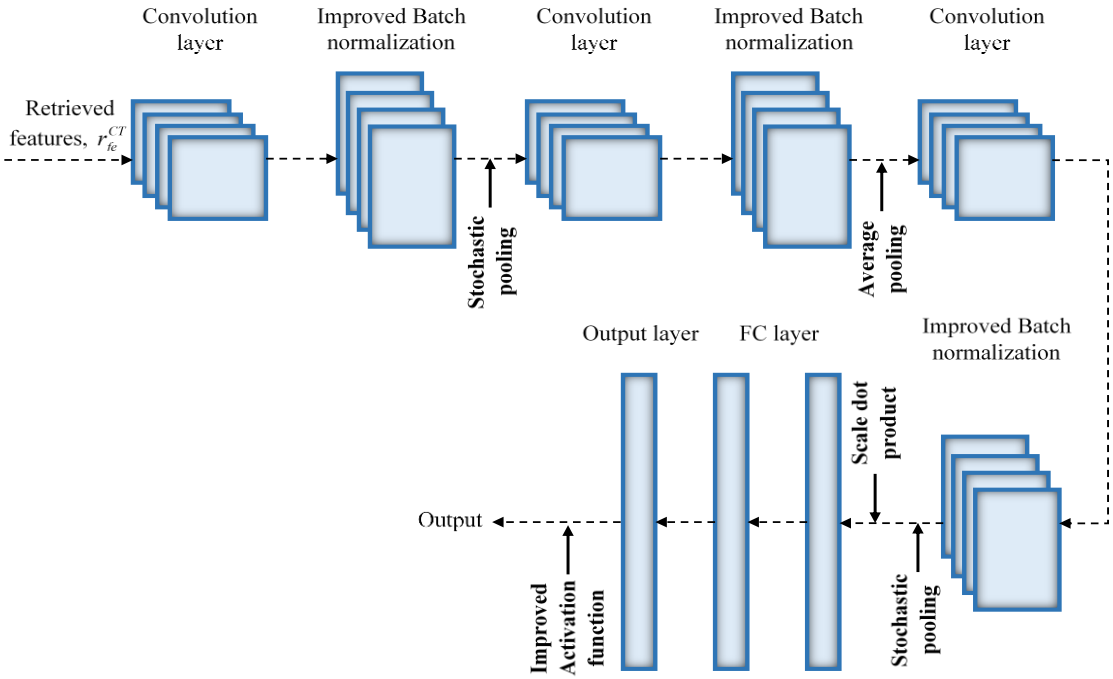

Figure 7. Architecture of the Improved LeNet-5 model

c. Stochastic pooling: Stochastic pooling randomly selects activations within small regions of the input feature maps.
d. Average pooling: It divides the input feature maps into non-overlapping regions and computes the average activation within each region.
e. Scale dot product: This operation computes the dot product among the feature vectors of two sets of activations, possibly scaled by a learnable parameter.
f. FC layer: It establishes connections among each neuron in the preceding layer with every neuron in the following layer, performing a matrix multiplication followed by a bias addition.
g. Improved activation function: Conventionally, it applies the SoftMax activation but it may not provide as smooth a gradient throughout its range compared to other activation functions, potentially leading to slower or less stable training of NN. Hence, the FC layer employs the Hard Elish Swish maxout activation, ensuring a smooth gradient across its range and enhancing the stability and efficiency of NN training [43]. Thus, the improved activation function is given in (25).

$$F(z) = \begin{cases} z \times max\left(0, min\left(1, \left(\frac{z+1}{2}\right)\right)\right), z > 0 \\ \left\{\frac{z}{1+e^{-z}} + max(w_1^t z + g_1, w_2^t z + g_2)\right\}, 0 \geq z \geq -1 \\ e^z - 1 * max\left(0, min\left(1, \left(\frac{z+1}{2}\right)\right)\right), otherwise \end{cases} \quad (25)$$

Consequently, the output achieved from this ILeNet-5 model is specified as ILe^{CT}.

3.5.2. Architecture of SqueezeNet model

SqueezeNet is a DNN architecture [44], which is characterized by convolutional layers, max pooling layers, fire modules, global average pooling, and a SoftMax activation function as illustrated in Figure 8.

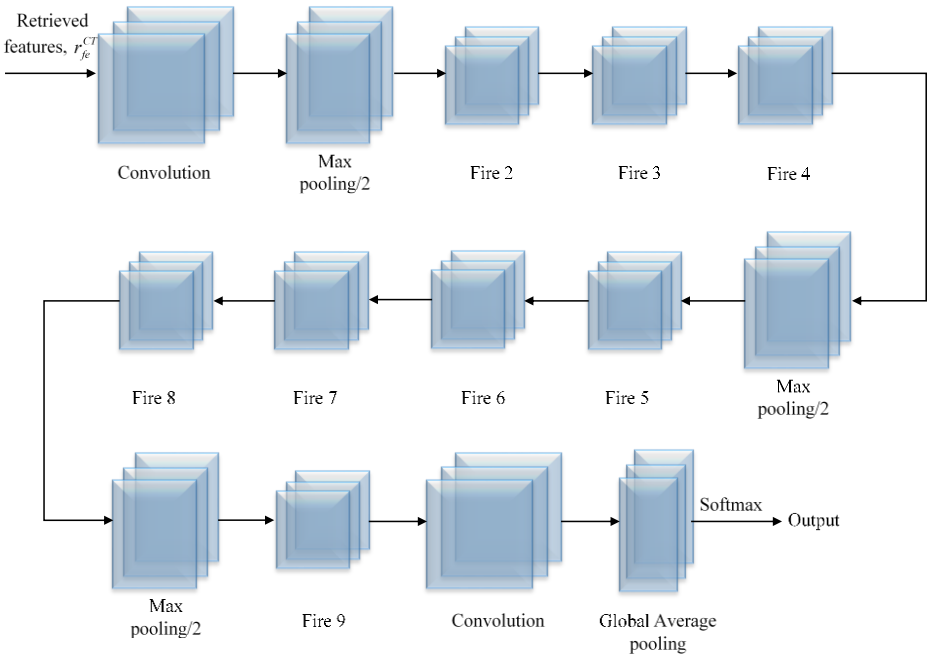

Figure 8. Architecture of the SqueezeNet model

Initially, the convolutional layers serve to extract meaningful features from the input retrieved features r_{fe}^{CT}, capturing important patterns and structures indicative of lung cancer. Subsequent max pooling layers downsampling the feature maps to decrease the computational complexity and enhance computational efficiency. Finally, the SoftMax classifier provides probabilistic predictions, assigning a probability distribution over the possible classes of lung cancer. Thus, the output obtained from this SqueezeNet is denoted as Sq^{CT}.

We have taken average of the outcomes of both ILeNet-5 model and SqueezeNet model to obtain the final classification result. By averaging the output of both classifiers, accurate classification output, which are the class labels like adenocarcinoma (1) or large cell carcinoma (2) or squamous cell carcinoma (3) or normal (0) are obtained.

4. RESULTS AND DISCUSSION

4.1. Simulation procedure

The Cloud-IoT based lung cancer classification and recommendation system was proposed in this study underwent simulation using Python, specifically utilizing Python version "3.7." The computational processing was conducted on an Intel(R) Core (TM) i5-4210U CPU @ 1.70 GHz processor, with 8.00 GB of installed RAM. The classification of lung cancer was performed through the analysis of chest CT-scan images dataset [45]. Additionally, we have conducted a cross validation for ILeS-Net model using lung cancer dataset [46].

4.2. Dataset description

This chest CT-scan images dataset (Database -1 or DB-1) includes 1000 CT scan images of 3 cancer types like large cell carcinoma (LCC) (338), adenocarcinoma (215) and squamous cell carcinoma (SCC) (260) along with the CT-scan images of normal chests (187) to accurately categorize or differentiate the normal lung nodules from the infected ones. Moreover, only for cross validation of ILeS-Net, we have utilized this lung cancer dataset (DB-2). This DB-2 includes 4598 CT-Scan images. From them, 3002 images belong to adenocarcinoma, 529 images belong to LCC, 355 images belong to SCC, while 712 were normal chest images.

4.3. Performance analysis

A comprehensive investigation was undertaken to evaluate the effectiveness of ILeS-Net and conventional methods within a Cloud-IoT-based system for the classification and recommendation of lung cancer. The evaluation incorporated numerous pivotal measures, including "Sensitivity, false negative rate (FNR), negative predictive value (NPV), specificity, false discovery rate (FDR), F-measure, precision, Matthews correlation coefficient (MCC), and accuracy." Moreover, the examination incorporated statistical analysis and ablation study. The ILeS-Net approach was compared against state-of-the-art techniques such as Lung-EffNet, SVM, Swin Transformer and CNN-ViT as well as traditional classifiers including LeNet, SqueezeNet, LinkNet, DCNN, and DBN. Both the ILeS-Net and conventional strategies were estimated using chest CT-scan images dataset. Additionally, Figure 9 depicts the input images alongside the pre-processed images obtained through Gaussian filtering. Specifically, Figure 9(a) displays the raw chest CT-scan images directly from the dataset, which serve as the initial input. Meanwhile, Figure 9(b) illustrates the corresponding pre-processed images after applying the Gaussian filter, demonstrating a reduction in image noise to improve the quality for the subsequent classification steps.

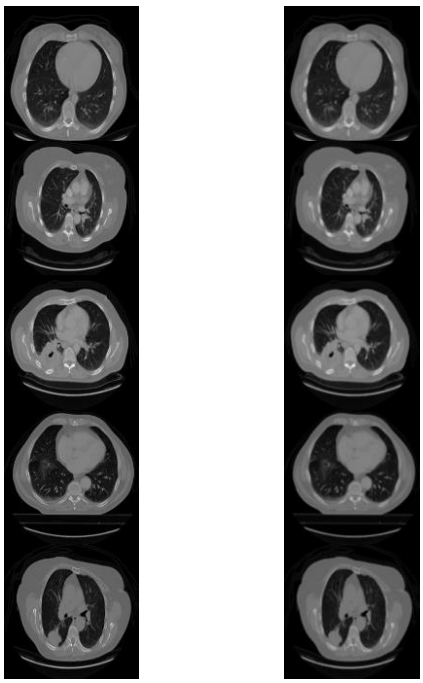

(a) (b)

Figure 9. Images for lung cancer classification (a) input images and (b) Gaussian filtering using pre-processed images

4.4. Segmentation analysis on I-BIRCH

In Figure 10, a visual representation of input images alongside segmented images is provided for various lung cancer classification approaches, including fuzzy C-means (FCM), conventional BIRCH, k-means, and I-BIRCH. Specifically, Figure 10(a) displays the original input images, while Figures 10(b) to 10(d) illustrate the segmentation results generated by FCM, conventional BIRCH, and k-means, respectively. Furthermore, Figure 10(e) showcases the distinct segmentation outcomes produced by the proposed I-BIRCH

method. This suggests that I-BIRCH effectively captures the relevant features necessary for accurate lung cancer classification, surpassing the performance of traditional segmentation approaches. The visual comparison presented in Figure 10 underscores the capability of I-BIRCH as a robust method for improving the exactness and reliability of lung cancer classification through precise image segmentation.

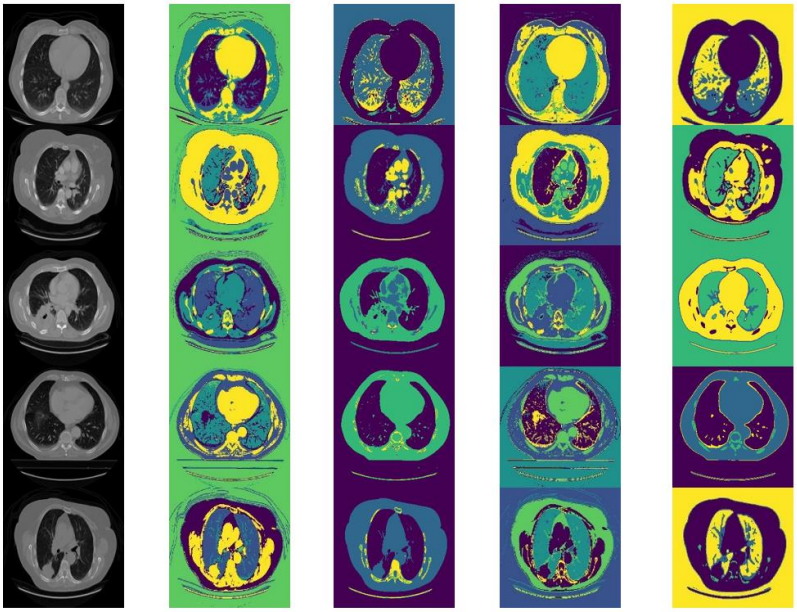

Figure 10. Images for lung cancer classification (a) input images, (b) FCM, (c) conventional BIRCH, (d) k-means and (e) I-BIRCH

The Dice coefficient, also known as the Dice similarity coefficient or Dice index, is a statistical measure used to quantify the similarity between two sets of data. The Dice coefficient is computed using (18):

$$DSC(N,O) = \frac{2(N \cap O)}{(N+O)} \tag{18}$$

Similarly, "The Jaccard coefficient, also known as the Jaccard similarity coefficient or Jaccard index, is a statistical measure used to evaluate the similarity and intersection between two sets of data." As well, it can be expressed as:

$$J(N,O) = \frac{|N \cap O|}{|N \cup O|} \tag{19}$$

In image segmentation evaluation, "N" typically signifies the ground truth segmented image, while "O" is employed for the predicted segmented image.

Table 1 offers an evaluation of segmentation by comparing the effectiveness of FCM, k-means, Conventional BIRCH, and I-BIRCH methods using various key metrics. Nonetheless, the standout performer proves to be the I-BIRCH method, outperforming all others with a Dice coefficient of 0.871, a Jaccard coefficient of 0.940, and a segmentation accuracy of 0.950. The results highlight the significant enhancements achieved by the I-BIRCH method, making it a compelling choice for accurate and reliable segmentation in image processing applications

Table 1. Segmentation assessment on I-BIRCH

Metrics	FCM	I-BIRCH	K-means	Conventional BIRCH
Dice	0.706	0.871	0.643	0.758
Jaccard	0.725	0.940	0.666	0.832
Segmentation Accuracy	0.763	0.950	0.676	0.855

4.5. Comparative evaluation in terms of positive metrics

The effectiveness of ILeS-Net scheme for lung cancer classification in a Cloud-IoT framework lies in its ability to achieve superior performance metrics compared to established methodologies. In Figure 11, a comparative analysis of the positive metric assessment of the ILeS-Net scheme. The Figure 11(a) presents a comprehensive analysis of the accuracy scores across different training data percentages for various models, including LeNet, SqueezeNet, LinkNet, DCNN, DBN, Lung-EffNet, SVM, Swin Transformer, CNN-ViT and the ILeS-Net approach. While DBN, Lung-EffNet, Swin Transformer and CNN-ViT exhibit moderate scores, peaking at 0.783, 0.803,0.813, and 0.820 respectively, SVM lags slightly behind with scores ranging from 0.598 to 0.738. Furthermore, the remaining subfigures explicitly depict the comparative results for other crucial positive metrics: Figure 11(b) illustrates precision, Figure 11(c) displays the F-measure, and Figure 11(d) showcases the Matthews correlation coefficient (MCC) across the varying percentages of training data.

As the percentage of training data improves, the precision of ILeS-Net model continues to improve, reaching a peak precision of 0.905 with 90% of the data. The integration of the Improved LGXP technique and hybrid model has not only enhanced accuracy but also elevated sensitivity, specificity, precision, and overall classification efficacy.

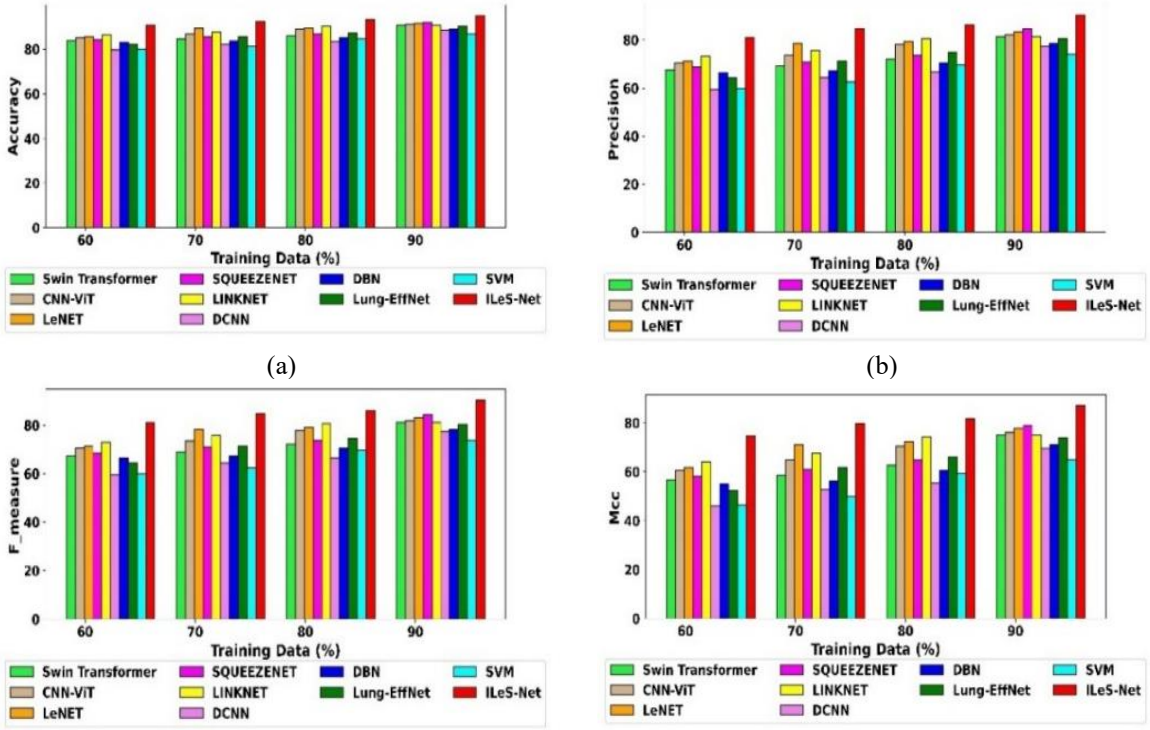

Figure 11. Positive metric assessment on ILeS-Net and traditional methods (a) accuracy, (b) precision, (c) F measure, (d) MCC

4.6. Ablation study of ILeS-Net

Table 2 presents an ablation study on ILeS-Net model, examining its performance compared to different scenarios like model without pre-processing, model without segmentation, model with conventional segmentation, model with conventional LGXP and model with conventional features. Among the scenarios, the model without pre-processing achieves a specificity of 0.938, model without segmentation achieves a specificity of 0.930, model employing conventional segmentation achieves a specificity of 0.934, while the one utilizing conventional LGXP achieves a slightly higher specificity of 0.939. On the other hand, utilizing conventional features leads to a higher FPR of 0.074, suggesting a relatively greater rate of false positive predictions. Notably, the ILeS-Net stands out with the lowest FPR of 0.051, highlighting its superior capacity to diminish false positive errors.

Table 2. Ablation analysis on ILeS-Net, model with conventional segmentation, model with conventional LGXP and model with conventional features

Metrics	Model without pre-processing	Model without segmentation	Model with conventional segmentation	Model with conventional LGXP	Model with conventional features	ILeS-Net
Accuracy	0.907	0.895	0.901	0.908	0.889	0.924
FPR	0.062	0.070	0.066	0.061	0.074	0.051
Specificity	0.938	0.930	0.934	0.939	0.926	0.949
F-measure	0.814	0.790	0.803	0.816	0.778	0.848
FNR	0.187	0.210	0.198	0.185	0.223	0.153
Sensitivity	0.813	0.790	0.802	0.815	0.777	0.847
MCC	0.752	0.720	0.737	0.755	0.703	0.797
Precision	0.814	0.791	0.803	0.817	0.778	0.848
NPV	0.938	0.930	0.949	0.938	0.926	0.949

4.7. K-fold validation assessment

Table 3 shows the cross-validation evaluation ofILeS-Net model over other models like LeNet, SqueezeNet, LinkNet, DCNN, DBN, Lung-EffNet, SVM, Swin Transformer, CNN-ViT and compared it with ILeS-Net model. This k-fold cross-validation is a method, which analyses the model's generalization and robustness to prevent overfitting. The ILeS-Net model outperforms all traditional models across all k-folds, proving its accuracy and effectiveness. For fold-1, ILeS-Net model attained greater accuracy of 0.945, while Swin Transformer, CNN-ViT, LeNet, SqueezeNet, LinkNet, DCNN, DBN, Lung-EffNet and SVM models attained the rates of 0.872, 0.855, 0.917, 0.902, 0.872, 0.801, 0.872, 0.874 and 0.930. For other folds also ILeS-Net model attained superior accuracy value, that proved this model's generalization and robustness.

Table 3. K-fold validation analysis comparison of ILeS-Net model over other models

Folds	Swin transformer	CNN-ViT	LeNET	SqueezeNet	LinkNet	DCNN	DBN	Lung-EffNet	SVM	ILeS-Net Net
fold-1	0.872	0.855	0.917	0.902	0.872	0.801	0.872	0.874	0.930	0.945
fold-2	0.901	0.872	0.922	0.916	0.901	0.814	0.880	0.903	0.901	0.956
fold-3	0.877	0.849	0.930	0.915	0.871	0.794	0.907	0.877	0.917	0.944
fold-4	0.896	0.904	0.932	0.915	0.851	0.856	0.852	0.862	0.901	0.949
fold-5	0.856	0.892	0.921	0.901	0.851	0.854	0.900	0.866	0.871	0.951

4.8. Cross validation

The cross-validation computes how well the ILeS-Net model generalizes to new data and also analyze the model's ability to prevents overfitting. During the cross validation, for training the ILeS-Net model, DB-1 was utilized and for testing, DB-2 was utilized. Also, the performance analysis of ILeS-Net model during the cross validation was given in Table 4. Then, ILeS-Net model was trained with DB-2 and tested with DB-1. From both processes, better performance in terms of accuracy, MCC, specificity, sensitivity, precision, F-measure, FPR, FNR, and NPV were obtained, which proved the ILeS-Net model's adaptability to different datasets.

Table 4. Analysis on the performance ofILeS-Net model for different datasets

Metrices	Cross validation (Train DB-1 and test DB-2)	Cross validation (Train DB-2 and test DB-1)
Accuracy	0.940	0.940
Sensitivity	0.894	0.885
Specificity	0.951	0.958
Precision	0.898	0.888
F_measure	0.896	0.887
MCC	0.858	0.848
NPV	0.949	0.956
FPR	0.049	0.042
FNR	0.106	0.115

4.9. Computational complexity

Table 5 shows that the comparison of different methods used in the lung cancer classification framework shows that the traditional Birch segmentation method requires 8.25656 seconds, while the improved I-Birch method takes slightly longer at 9.55565 seconds due to its enhanced clustering accuracy and adaptive thresholding features. For feature extraction, the LGXP method operates faster at 2.9154 seconds, whereas the Improved ILGXP method takes a bit more time, 3.318999 seconds, reflecting

the additional processing needed to enhance texture pattern recognition. These values indicate a trade-off between computational complexity and improved performance in the proposed methods.

Table 5. Analysis of computational time

Methods	Computing Time (sec)
Birch	8.25656
IBirch	9.55565
LGXP	2.9154
ILGXP	3.318999

5. CONCLUSION

This study presents a Cloud-IoT based lung cancer classification and recommendation system using the hybrid ILeS-Net model. By integrating improved segmentation (I-BIRCH), enhanced feature extraction (I-LGXP), and a hybrid CNN architecture, the system demonstrated high accuracy in CT image-based lung cancer detection, achieving up to 0.951 with 90% training data. Cloud-IoT integration ensures scalable, real-time decision support for healthcare providers. While the results confirm the effectiveness of the approach, further validation on larger, multi-institutional datasets and comparisons with state-of-the-art deep learning models are necessary. Future work will focus on expanding the recommendation module, incorporating genomic data, and deploying the system in real-world clinical environments. Replication of results: The source code link is *https://github.com/affrose1/ILeS-Net-model*.

ACKNOWLEDGMENTS

The authors would like to thank all individuals who contributed to this research work through technical support, guidance, and valuable discussions. Special thanks are extended to colleagues and institutional staff who assisted in data collection and system implementation. All acknowledged individuals have provided their consent for inclusion in this section.

FUNDING INFORMATION

The authors state that no external funding was received for this research work.

AUTHOR CONTRIBUTIONS STATEMENT

This journal uses the Contributor Roles Taxonomy (CRediT) to recognize individual author contributions, reduce authorship disputes, and facilitate collaboration.

Name of Author	C	M	So	Va	Fo	I	R	D	O	E	Vi	Su	P	Fu
Affrose	✓	✓	✓	✓										
Cheruku Sandesh Kumar						✓	✓	✓	✓					
Archek Praveen Kumar									✓	✓	✓	✓	✓	✓

C : **C**onceptualization
M : **M**ethodology
So : **So**ftware
Va : **Va**lidation
Fo : **Fo**rmal analysis
I : **I**nvestigation
R : **R**esources
D : **D**ata Curation
O : Writing - **O**riginal Draft
E : Writing - Review & **E**diting
Vi : **Vi**sualization
Su : **Su**pervision
P : **P**roject administration
Fu : **Fu**nding acquisition

CONFLICT OF INTEREST STATEMENT

The authors declare that they have no known competing financial interests or personal relationships that could have appeared to influence the work reported in this paper. Authors state no conflict of interest.

INFORMED CONSENT

Not Applicable

ETHICAL APPROVAL

There is no ethical consideration of this work.

DATA AVAILABILITY

The datasets used in this study are publicly available and can be accessed from the following sources:

- Chest CT scan images dataset: Available at *https://www.kaggle.com/datasets/mohamedhanyyy/chest-ctscan-images* (accessed in December 2025),
- Lung cancer dataset: Available at *https://universe.roboflow.com/lung-cancer-3gsnq/lung-cancer-dataset* (accessed in December 2025).

The authors confirm that the data supporting the findings of this study are openly available from these repositories.

REFERENCES

[1] A. U. R. Butt *et al.*, "An optimized role-based access control using trust mechanism in e-health cloud environment," *IEEE Access*, vol. 11, pp. 138813–138826, 2023, doi: 10.1109/ACCESS.2023.3335984.

[2] K. M. Hassan, A. Abdo, and A. Yakoub, "Enhancement of health care services based on cloud computing in IoT environment using hybrid swarm intelligence," *IEEE Access*, vol. 10, pp. 105877–105886, 2022, doi: 10.1109/ACCESS.2022.3211512.

[3] R. R. Irshad *et al.*, "A multi-objective bee foraging learning-based particle swarm optimization algorithm for enhancing the security of healthcare data in cloud system," *IEEE Access*, vol. 11, pp. 113410–113421, 2023, doi: 10.1109/ACCESS.2023.3265954.

[4] S. Ali *et al.*, "Towards pattern-based change verification framework for cloud-enabled healthcare component-based," *IEEE Access*, vol. 8, pp. 148007–148020, 2020, doi: 10.1109/ACCESS.2020.3014671.

[5] S. Fugkeaw, L. Wirz, and L. Hak, "Secure and lightweight blockchain-enabled access control for fog-assisted IoT cloud based electronic medical records sharing," *IEEE Access*, vol. 11, pp. 62998–63012, 2023, doi: 10.1109/ACCESS.2023.3288332.

[6] S. Wankhade and V. S., "A novel hybrid deep learning method for early detection of lung cancer using neural networks," *Healthcare Analytics*, vol. 3, p. 100195, Nov. 2023, doi: 10.1016/j.health.2023.100195.

[7] I. Nazir, I. U. Haq, S. A. Alqahtani, M. M. Jadoon, and M. Dahshan, "Machine learning-based Lung cancer detection using multiview image registration and fusion," *Journal of Sensors*, vol. 2023, p. 6683438, 2023, doi: 10.1155/2023/6683438.

[8] K. Zala, H. K. Thakkar, R. Jadeja, P. Singh, K. Kotecha, and M. Shukla, "PRMS: Design and development of patients' e-healthcare records management system for privacy preservation in third party cloud platforms," *IEEE Access*, vol. 10, pp. 85777–85791, 2022, doi: 10.1109/ACCESS.2022.3198094.

[9] L. Wang, "Deep learning techniques to diagnose lung cancer," *Cancers*, vol. 14, no. 22, p. 5569, 2022, doi: 10.3390/cancers14225569.

[10] B. S. Deepapriya *et al.*, "Performance evaluation of deep learning techniques for lung cancer prediction," *Soft Computing*, vol. 27, no. 13, pp. 9191–9198, 2023, doi: 10.1007/s00500-023-08313-7.

[11] M. Anuradha *et al.*, "IoT enabled cancer prediction system to enhance the authentication and security using cloud computing," *Microprocessors and Microsystems*, vol. 80, Feb. 2021, doi: 10.1016/j.micpro.2020.103301.

[12] A. R. Wahab Sait, "Lung cancer detection model using deep learning technique," *Applied Sciences (Switzerland)*, vol. 13, no. 22, p. 12510, 2023, doi: 10.3390/app132212510.

[13] C. Venkatesh, K. Ramana, S. Y. Lakkisetty, S. S. Band, S. Agarwal, and A. Mosavi, "A neural network and optimization based lung cancer detection system in CT images," *Frontiers in Public Health*, vol. 10, p. 769692, 2022, doi: 10.3389/fpubh.2022.769692.

[14] J. Zaki, S. M. R. Islam, N. S. Alghamdi, M. Abdullah-Al-Wadud, and K. S. Kwak, "Introducing cloud-assisted micro-service-based software development framework for healthcare systems," *IEEE Access*, vol. 10, pp. 33332–33348, 2022, doi: 10.1109/ACCESS.2022.3161455.

[15] D. N. Sachin, B. Annappa, S. Hegde, C. S. Abhijit, and S. Ambesange, "FedCure: A heterogeneity-aware personalized federated learning framework for intelligent healthcare applications in IoMT environments," *IEEE Access*, vol. 12, pp. 15867–15883, 2024, doi: 10.1109/ACCESS.2024.3357514.

[16] M. M. Islam and Z. A. Bhuiyan, "An integrated scalable framework for cloud and IoT based green healthcare system," *IEEE Access*, vol. 11, pp. 22266–22282, 2023, doi: 10.1109/ACCESS.2023.3250849.

[17] T. Muhammed, R. Mehmood, A. Albeshri, and I. Katib, "UbeHealth: A personalized ubiquitous cloud and edge-enabled networked healthcare system for smart cities," *IEEE Access*, vol. 6, pp. 32258–32285, 2018, doi: 10.1109/ACCESS.2018.2846609.

[18] N. Faruqui, M. A. Yousuf, F. A. Kateb, M. Abdul Hamid, and M. M. Monowar, "Healthcare as a service (HAAS): CNN-based cloud computing model for ubiquitous access to lung cancer diagnosis," *Heliyon*, vol. 9, no. 11, p. e21520, Nov. 2023, doi: 10.1016/j.heliyon.2023.e21520.

[19] S. Tomassini *et al.*, "On-cloud decision-support system for non-small cell lung cancer histology characterization from thorax computed tomography scans," *Computerized Medical Imaging and Graphics*, vol. 110, p. 102310, Dec. 2023, doi: 10.1016/j.compmedimag.2023.102310.

[20] E. J. Hwang, J. M. Goo, H. Y. Kim, J. Yi, S. H. Yoon, and Y. Kim, "Implementation of the cloud-based computerized interpretation system in a nationwide lung cancer screening with low-dose CT: comparison with the conventional reading system," *European Radiology*, vol. 31, no. 1, pp. 475–485, 2021, doi: 10.1007/s00330-020-07151-7.

[21] A. Masood *et al.*, "Cloud-based automated clinical decision support system for detection and diagnosis of Lung cancer in chest CT," *IEEE Journal of Translational Engineering in Health and Medicine*, vol. 8, pp. 1–13, 2020, doi: 10.1109/JTEHM.2019.2955458.

[22] G. Kasinathan and S. Jayakumar, "Cloud-based Lung Tumor detection and stage classification using deep learning techniques," *BioMed Research International*, vol. 2022, p. 17, 2022, doi: 10.1155/2022/4185835.

[23] D. Valluru and I. J. S. Jeya, "IoT with cloud based lung cancer diagnosis model using optimal support vector machine," *Health Care Management Science*, vol. 23, no. 4, pp. 670–679, 2020, doi: 10.1007/s10729-019-09489-x.

[24] A. Masood *et al.*, "Automated decision support system for Lung Cancer detection and classification via enhanced RFCN with multilayer fusion RPN," *IEEE Transactions on Industrial Informatics*, vol. 16, no. 12, pp. 7791–7801, 2020, doi: 10.1109/TII.2020.2972918.
[25] S. Mishra, H. K. Thakkar, P. K. Mallick, P. Tiwari, and A. Alamri, "A sustainable IoHT based computationally intelligent healthcare monitoring system for lung cancer risk detection," *Sustainable Cities and Society*, vol. 72, p. 103079, 2021, doi: 10.1016/j.scs.2021.103079.
[26] R. Raza *et al.*, "Lung-EffNet: Lung cancer classification using EfficientNet from CT-scan images," *Engineering Applications of Artificial Intelligence*, vol. 126, 2023, doi: 10.1016/j.engappai.2023.106902.
[27] F. S. Gomiasti, W. Warto, E. Kartikadarma, J. Gondohanindijo, and D. R. I. M. Setiadi, "Enhancing Lung cancer classification effectiveness through hyperparameter-tuned support vector machine," *Journal of Computing Theories and Applications*, vol. 1, no. 4, pp. 396–406, 2024, doi: 10.62411/jcta.10106.
[28] M. M. Amin, A. S. Ismail, and M. E. Shaheen, "Multimodal non-small cell lung cancer classification using convolutional neural networks," *IEEE Access*, vol. 12, pp. 134770–134778, 2024, doi: 10.1109/ACCESS.2024.3461878.
[29] M. D. Z. I. Noman, K. Sati, M. A. Yousuf, S. Aloteibi, and M. A. Moni, "LungCT-NET: An explainable transfer learning-based robust ensemble model for lung cancer diagnosis," *Knowledge-Based Systems*, vol. 324, 2025, doi: 10.1016/j.knosys.2025.113854.
[30] K. Zhao, Y. Si, L. Sun, and X. Meng, "PortNet: Achieving lightweight architecture and high accuracy in lung cancer cell classification," *Heliyon*, vol. 11, no. 3, 2025, doi: 10.1016/j.heliyon.2025.e41850.
[31] R. Sun, Y. Pang, and W. Li, "Efficient Lung cancer image classification and segmentation algorithm based on an improved Swin Transformer," *Electronics (Switzerland)*, vol. 12, no. 4, 2023, doi: 10.3390/electronics12041024.
[32] M. Imran, B. Haq, E. Elbasi, A. E. Topcu, and W. Shao, "Transformer based hierarchical model for non-small cell lung cancer detection and classification," *IEEE Access*, vol. 12, pp. 145920–145933, 2024, doi: 10.1109/ACCESS.2024.3449230.
[33] G. P. Kumar, "Analysis of visibility improvement based on Gaussian/bilateral filter," *International Journal of Analytical and Experimental Modal Analysis*, vol. IX, no. XII, pp. 16–19, 2021.
[34] D. Li and Y. Wang, "Application of an improved threshold segmentation method in SEM material analysis," in *IOP Conference Series: Materials Science and Engineering*, 2018, vol. 322, no. 2, p. 22057, doi: 10.1088/1757-899X/322/2/022057.
[35] D. R. Wilson and T. R. Martinez, "Improved heterogeneous distance functions," *Journal of Artificial Intelligence Research*, vol. 6, pp. 1–34, 1997, doi: 10.1613/jair.346.
[36] J. A. Almaraz-Damian, V. Ponomaryov, S. Sadovnychiy, and H. Castillejos-Fernandez, "Melanoma and nevus skin lesion classification using handcraft and deep learning feature fusion via mutual information measures," *Entropy*, vol. 22, no. 4, 2020, doi: 10.3390/E22040484.
[37] I. A. Kamanga, "Improved edge detection using variable thresholding technique and convolution of Gabor with Gaussian filters," *Signal & Image Processing : An International Journal*, vol. 13, no. 5, pp. 1–15, 2022, doi: 10.5121/sipij.2022.13501.
[38] Z. R. Tan, S. Tian, and C. L. Tan, "Using pyramid of histogram of oriented gradients on natural scene text recognition," in *2014 IEEE International Conference on Image Processing, ICIP 2014*, 2014, pp. 2629–2633, doi: 10.1109/ICIP.2014.7025532.
[39] X. Zenggang, T. Zhiwen, C. Xiaowen, Z. Xue-min, Z. Kaibin, and Y. Conghuan, "Research on image retrieval algorithm based on combination of color and shape features," *Journal of Signal Processing Systems*, vol. 93, no. 2–3, pp. 139–146, Mar. 2021, doi: 10.1007/s11265-019-01508-y.
[40] M. Keivani, J. Mazloum, E. Sedaghatfar, and M. B. Tavakoli, "Automated analysis of leaf shape, texture, and color features for plant classification," *Traitement du Signal*, vol. 37, no. 1, pp. 17–28, 2020, doi: 10.18280/ts.370103.
[41] S. Balasubramaniam, Y. Velmurugan, D. Jaganathan, and S. Dhanasekaran, "A modified LeNet CNN for breast cancer diagnosis in ultrasound images," *Diagnostics*, vol. 13, no. 17, 2023, doi: 10.3390/diagnostics13172746.
[42] J. Bjorck, C. Gomes, B. Selman, and K. Q. Weinberger, "Understanding batch normalization," *Advances in Neural Information Processing Systems*, vol. 2018-December, pp. 7694–7705, 2018.
[43] C. Nwankpa, W. Ijomah, A. Gachagan, and S. Marshall, "Activation functions: Comparison of trends in practice and research for deep learning," *arXiv preprint arXiv:1811.03378*, Nov. 2018, [Online]. Available: http://arxiv.org/abs/1811.03378.
[44] L. S. Bernardo, R. Damaševičius, S. H. Ling, V. H. C. de Albuquerque, and J. M. R. S. Tavares, "Modified SqueezeNet architecture for Parkinson's disease detection based on keypress data," *Biomedicines*, vol. 10, no. 11, 2022, doi: 10.3390/biomedicines10112746.
[45] M. Hany, "Chest CT-Scan images Dataset," *kaggle.com*, 2020. https://www.kaggle.com/datasets/mohamedhanyyy/chest-ctscan-images (accessed Dec. 01, 2025).
[46] Roboflow Universe, "Lung cancer dataset," *universe.roboflow.com*, 2025. https://universe.roboflow.com/lung-cancer-3gsnq/lung-cancer-dataset/browse?queryText=&pageSize=50&startingIndex=0&browseQuery=true (accessed Dec. 01, 2025).

BIOGRAPHIES OF AUTHORS

Affrose research scholar at Amity University Rajasthan, Jaipur, India. Her research areas are IoT, image processing and machine learning. She holds B.Tech. (ECE), M.Tech. (VLSI) from JNTUH University. Her areas of interest are image processing, IoT, and ML. She has published few papers on my research work. She can be contacted at email: roseaffrose557@gmail.com.

Cheruku Sandesh Kumar presently serving as a distinguished assistant professor in Electronics and Communication Engineering Department at Amity University Rajasthan, Jaipur, India, is renowned for his outstanding contributions in the fields of image processing. He earned his Ph.D. in electronics and communication engineering from Amity University Rajasthan. Dr. Cheruku Sandesh Kumar has contributed significantly to research. His scholarly endeavors include the publication of various papers in indexed international and national journals, alongside editorial responsibilities for several international journals. He has authored several books in the field of electronics and has supervised numerous major and mini projects for undergraduate, postgraduate, and PhD scholars. He can be contacted at email: sandeshkumarc7@gmail.com.

Archek Praveen Kumar presently serving as a distinguished professor and Head of the Electronics and Communication Engineering Department at Gates Institute of Technology, is renowned for his outstanding contributions in the fields of signal processing and image processing. He earned his Ph.D. in electronics and communication engineering from Amity University Rajasthan in 2017, M.Tech. in digital electronics and advanced communication from Manipal University Karnataka in 2009, and B.E. in electronics and communication engineering from Anna University Chennai in 2006. He has contributed significantly to research, having filed 4 patents in the domains of medical and signal processing. He can be contacted at email: archekpraveen@gmail.com.